Korean J. Chem. Eng., 37(12), 2359-2367 (2020)
DOI: 10.1007/s11814-020-0705-0

pISSN: 0256-1115
eISSN: 1975-7220

Free-standing Ag nanoparticle-decorated MoS_2 microflowers grown on carbon cloth for photocatalytic oxidation of Rhodamine B

Sangeeta Adhikari*,‡, Sandip Mandal,‡, and Do-Heyoung Kim*,†**

*School of Chemical Engineering, Chonnam National University, 77, Yongbong-ro, Buk-gu, Gwangju 61186, Korea
**Department of Environment and Energy Engineering, Chonnam National University, 77, Yongbong-ro, Buk-gu, Gwangju 61186, Korea
(*Received 11 September 2020 • Revised 19 October 2020 • Accepted 2 November 2020*)

Abstract−MoS_2 microflowers were grown on the surface of a carbon cloth (CC) via a one-step hydrothermal method. Sodium borohydride was used to chemically reduce Ag nanoparticles on the surface of the as-grown MoS_2 microflowers. The Ag nanoparticle-decorated MoS_2 microflowers grown on the CC (Ag@MoS_2/CC) were used for the photocatalytic degradation of rhodamine B (RB) via visible light absorption. The Ag nanoparticles significantly affected the reactivity of the photocatalyst by generating a large number of oxidative radical species. The catalytic reaction followed first-order kinetics and the rate of degradation improved by about 3.3 times upon the deposition of Ag nanoparticles on the surface. Scavenger experiments showed that the hydroxyl radicals generated by the photogenerated electrons were the main contributing species in the degradation of RB. The catalytic mechanism involved efficient electron transfer from the conduction band of MoS_2 to Ag through a space charge region, making the surface of the photocatalyst highly electron populated. The fabricated catalyst was highly stable for multiple experiments.

Keywords: Carbon Cloth, MoS_2 Microflowers, Ag Nanoparticles, Rhodamine B, Hydroxyl Radicals

INTRODUCTION

Over the last few decades, various efforts have been made to design nanomaterials for solving problems of environmental pollution and the energy crisis [1]. The progress in developing novel materials and improving their properties has been documented in various review articles [2-4]. It is worth pointing out that the majority of environmental hazards are due to the lack of standardization of waste management systems, especially in water. Excessive discharge of highly stable and soluble organic/inorganic components into waterbodies has led to enormous long-term health issues [5,6]. Various methods such as homogeneous/heterogeneous photocatalysis [7,8], photoelectrocatalysis [9], adsorption [10], coagulation, and electro-oxidation [11] have been used to treat wastewater. Heterogeneous photocatalysis is a multifunctional method that has been extensively used for wastewater treatment, water splitting, and other air- and water-related problems [12-14]. Nanomaterials have been an important aspect in photocatalysis. Various nanomaterials have been investigated for the catalytic degradation of pollutants in wastewater [9,15,16].

A major challenge in the catalytic degradation of wastewater pollutants is the development of materials with visible light absorption and structural tuning properties [17-19]. In this context, MoS_2 has gained attention due to its interesting optoelectronic properties and visible light absorbance, and has been exploited for CO_2 reduction and wastewater treatment [20,21]. MoS_2 exhibits a unique two-dimensional (2D) layered structure with active sites at the edges and ease of dispersion [22-24]. However, it suffers from low charge carrier mobility due to rapid recombination [25]. In addition, MoS_2 exhibits poor catalytic performance because agglomeration of its 2D layers reduces its active surface area. To improve the performance of MoS_2 various approaches, such as the formation of binary/ternary layered heterojunctions [25], doping [26], impregnation, and surface modification [27], are used to hinder its active charge carrier stimulation. Moreover, the poor recyclability of powder catalysts also limits their practical application. Hence, the use of substrates for the growth of 2D layered catalysts not only improves their recyclability (because of their free standing nature) but also enhances the surface utility of the layered 2D structures by preventing agglomeration [28]. Fluorine- and indium-doped tin oxide are the most widely used substrates for the growth of free-standing catalysts [29,30]. Carbon cloth (CC) is another interesting flexible substrate to grow active catalysts [31]. Heterostructured MoS_2/SnO_2/CC photocatalysts have been developed for the visible-light photocatalytic degradation of rhodamine B (RB) [25]. CC with free-standing MoS_2/Bi_2S_3 has also been investigated as a novel filter membrane for the visible-light degradation of multiple organic and inorganic components under flowing conditions [32]. To increase the number of catalytic sites on MoS_2, various transition and noble metals have been incorporated into the host structure to facilitate the formation/separation of charge carriers. The motivation for the integration of metals on the surface of photocatalysts is to efficiently absorb the visible light and utilize it for increasing the number of catalytic sites [33,34]. Recently, it has been demonstrated that MoS_2 nanosheets modified with Ag show efficient visible-light water splitting and

†To whom correspondence should be addressed.
E-mail: kdhh@chonnam.ac.kr
‡Equal Contribution

hydrogen gas evolution [35,36].

In this study, MoS_2 microflowers have been grown on a CC substrate followed by modification to the surface of the microflowers with Ag nanoparticles using a borohydride reduction process. The performance of the resulting nano-composite material for the photocatalytic degradation of organic pollutant, rhodamine B was evaluated. The growth of MoS_2 on the CC substrate was confirmed by examining the structure, morphology, and optical properties of the catalyst. Photocatalytic degradation experiments revealed that the Ag nanoparticle-modification efficiently enhanced the structural and catalytic properties of the catalyst. Studies in relation to dye concentration and oxidizer effect have also been understood. The charge transfer mechanism of the designed catalyst was investigated and the mechanism has been deduced based on the scavenger experiments. The free-standing catalyst electrode was investigated for reusability through consecutive photochemical reactions.

EXPERIMENTAL PROCEDURE

1. Chemicals

All the chemicals used in this work were purchased from Sigma Aldrich and used without any further purification and treatment unless mentioned. The chemicals procured were of analytical grade. The purity was of thiourea (≥99.0%), silver nitrate (≥99.0%), and sodium borohydride (≥99.0%). Acetone, ethanol and hydrochloric acid were supplied by DAEJUNG, Republic of Korea. FC International supplied the carbon cloth (W0S1002, 360 μm).

2. Growth of MoS_2 Microflowers on CC

The MoS_2 microflowers on the CC substrate were grown using a facile one-step hydrothermal method. Prior to the growth of MoS_2 microflowers, the commercially obtained CC substrate (4 cm×4 cm) was treated with 1 M HCl followed by ultrasonication with acetone, ethanol, and distilled water. The cleaned CC was then dried in a hot air oven at 60 °C for 10 h. The precursor solution used for the growth of the MoS_2 microflowers was prepared by dissolving 1 mmol MoO_3 particles in 40 mL distilled water in a 100 mL beaker, where MoO_3 particles were synthesized by a procedure mentioned elsewhere [37]. The resulting solution was ultrasonicated for 60 min to obtain a homogeneous dispersion of MoO_3 particles. To the homogenized dispersion, 4 mmol thiourea was added and the reaction mixture was acidified using conc. HNO_3 until a pH value of ~2 was attained. The acidified precursor was magnetically stirred for about 2 h for homogeneous mixing of both the components to form the final precursor for the hydrothermal reaction. The mixture was then transferred to a clean Teflon beaker and the cleaned CC substrate was immersed into the solution. The Teflon beaker was placed in a stainless-steel autoclave and was then threaded tightly followed by autoclaving for 12 h at 200 °C. The autoclave was then cooled naturally and the MoS_2-grown CC was isolated by washing with water followed by drying overnight at 60 °C. The dried MoS_2/CC was then used directly for the analyses and further applications without any additional treatment. The weight of MoS_2 grown on the CC substrate was about 10 mg.

3. Deposition of Ag Nanoparticles on MoS_2/CC

The deposition of Ag on MoS_2/CC was carried out using a sodium borohydride reduction process. Two separate solutions of 0.05 mmol silver nitrate and 5 mmol sodium borohydride were prepared for the deposition process. First, MoS_2/CC was immersed into the Ag nitrate solution followed by drying at 70 °C on a hot plate for about 5 min. Then, the Ag ion-decorated MoS_2/CC was immersed in the sodium borohydride solution for the chemical reduction of Ag ions to Ag nanoparticles. After the reduction process, the Ag-decorated MoS_2/CC sample was water-jetted to remove excess boundless Ag ions. These steps for Ag deposition were repeated five times. Finally, prior to the physicochemical analyses and practical experiments, the as-obtained Ag@MoS_2/CC was heat-treated at 120 °C for removing impurities. The synthesis process used in this study is shown in Scheme 1.

4. Characterization

The X-ray diffraction patterns of pristine CC, MoS_2/CC, and Ag@MoS_2/CC were recorded on a PANalytical X-ray diffractometer (XRD). The micrographs of the as-grown MoS_2 and Ag@MoS_2/CC samples were obtained using a high-resolution field emission scan-

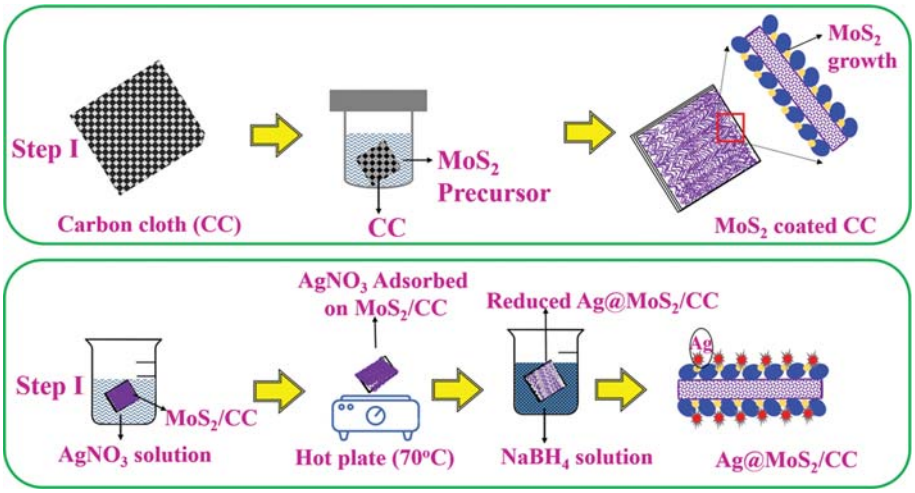

Scheme 1. Schematic illustration of the fabrication of Ag@MoS_2/CC- Step I: Hydrothermal growth of MoS_2 microflowers on CC and Step 2: Chemical reduction of Ag nanoparticles on MoS_2/CC.

ning electron microscope (HR-FESEM). Micrographs with detailed information on the structural features of the samples were recorded using a TECNAI G2 F20 transmission electron microscope (TEM). An ESCALAB-MKII X-ray photoelectron spectrophotometer (XPS) was used for analyzing the composition of $Ag@MoS_2/CC$. The optical properties of the as-synthesized samples were evaluated using a CARY-VARIAN UV-visible spectrophotometer.

5. Photochemical Experiments

Rhodamine B (RB) was used as the model pollutant for investigating the catalytic property of MoS_2/CC and $Ag@MoS_2/CC$. A stock solution of RB with a concentration of 10 ppm was prepared in distilled water. A 150-W Xe lamp with an AM 1.5G filter (HS Technologies, South Korea) was used as the visible light source. A two-step procedure was followed for the photochemical degradation of RB. Since, in this study, the catalysts were grown on a CC substrate, the catalysts and pollutant could be easily separated. First, the catalyst was immersed in a 30 mL solution of the pollutant in a quartz beaker under light irradiation. Then, the catalytically degraded pollutant was taken out from the beaker after fixed time intervals and analyzed using a UV-visible spectrophotometer. Before carrying out the catalytic experiments, the catalyst was immersed in the pollutant solution for about 60 min to achieve the adsorption-desorption equilibrium. The solution was irradiated after the adsorption process. The concentration of RB was monitored at the absorption wavelength maximum of 554 nm. Furthermore, the reactive species involved in the photochemical reaction were examined using 15 mM of chemical reagents such as benzoquinone (BQN), sodium oxalate (SO), and tert-butylalcohol (TBA).

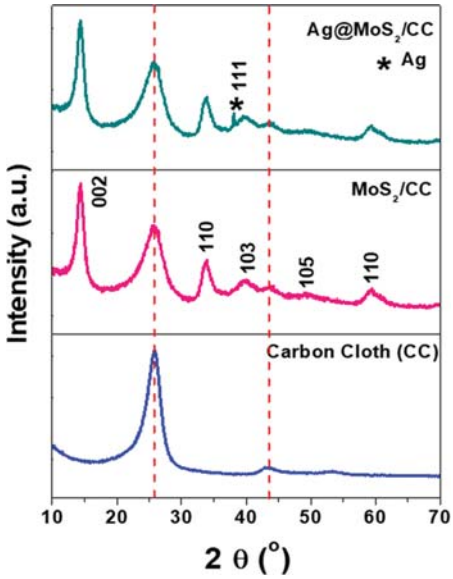

Fig. 1. X-ray diffraction patterns of carbon cloth (CC), as-grown MoS_2/CC, and as-deposited $Ag@MoS_2/CC$.

RESULTS AND DISCUSSION

1. Structural and Morphological Analysis

Fig. 1 shows the XRD patterns of pristine carbon cloth (CC), MoS_2/CC, and $Ag@MoS_2/CC$. The XRD peaks of MoS_2/CC could be indexed to the standard orthorhombic phase of MoS_2 with the

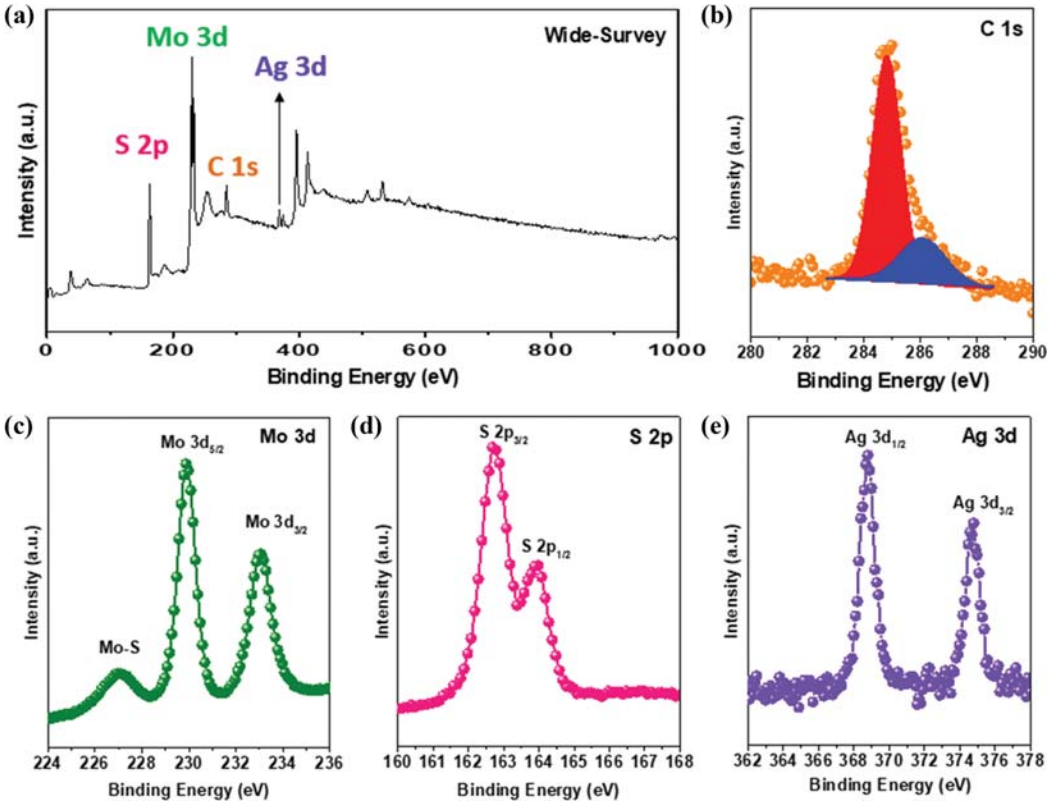

Fig. 2. (a) Wide survey scan of $Ag@MoS_2/CC$; (b) C 1s; (c) Mo 3d; (d) S 2p; and (e) Ag 3d XPS spectra of $Ag@MoS_2/CC$.

$P6_3/mmc$ space group having standard JCPDS card number 87-2416. MoS_2/CC showed XRD peaks at 2θ values=14.4, 32.6, 39.5, 49.8, and 60.4° corresponding to the (002), (100), (103), (105), and (110) planes of orthorhombic MoS_2, respectively. The few broad hump-like peaks can be attributed to the partial crystallinity or small domain size of the as-synthesized MoS_2 microflowers. In the case of Ag@MoS_2/CC sample, the peaks corresponding to Ag merged with those corresponding to MoS_2. However, a strong and distinct peak was observed at 38.11° corresponding to the (111) plane of cubic Ag. In both the growth and deposition processes, no other impurity was observed, indicating the high purity of the samples. Furthermore, compositional, elemental, and oxidation state analyses of Ag@MoS_2/CC were carried out with X-ray photoelectron spectroscopy.

Fig. 2(a) shows the wide survey scan of Ag@MoS_2/CC, showing its C1s, Mo3d, S2p, and Ag3d peaks. This indicates that the sample was highly pure. C 1s spectrum of the sample could be deconvoluted into two peaks at the binding energies of 284.68 and 286.08 eV (Fig. 2(b)) corresponding to adventitious carbon (C=C) and C-O-C binding, respectively [38]. Fig. 2(c) shows the Mo 3d XPS spectrum of Ag@MoS_2/CC with two doublets at 229.9 and 233.0 eV corresponding to the Mo $3d_{5/2}$ and $Mo3d_{3/2}$ orbitals, respectively. These peaks confirm the Mo^{4+} oxidation state of Mo3d in the Ag@MoS_2/CC sample. In addition, Mo-S peak centered at binding energy 226.8 eV was also observed. In addition, the high-resolution S 2p spectrum of the Ag@MoS_2/CC sample (Fig. 2(d)) showed two doublets at 162.7 and 163.9 eV corresponding to the S $2p_{3/2}$ and S $2p_{1/2}$ orbitals, respectively [39]. Thus, the peaks appeared because of S^{2-} bridging and the S^{2-} ligands from MoS_2. Fig. 2(e) shows the Ag 3d XPS spectrum of the Ag@MoS_2/CC sample. Zero-valent Ag peaks corresponding to Ag $3d_{5/2}$ and Ag $3d_{3/2}$ were observed at 368.6 and 374.8 eV, respectively [40]. The XPS results revealed that Ag was successfully deposited on the as-grown MoS_2 microflowers. According to XPS, the loading of silver in Ag@MoS_2/CC was found to be 2.28 atomic percent (2.28 at%).

Fig. 3 shows the FESEM images of MoS_2/CC and Ag@MoS_2/CC. It can be observed from Fig. 3(a) that each carbon fiber in the CC was well covered with the as-grown MoS_2 microflowers. Fig. 3(b) shows the zoomed-in image of a single carbon fiber. It can be observed clearly from the figure that the individual carbon fiber was completely covered with the grown MoS_2 microflowers. The MoS_2 microflowers show a thin sheet-like structure and self-assem-

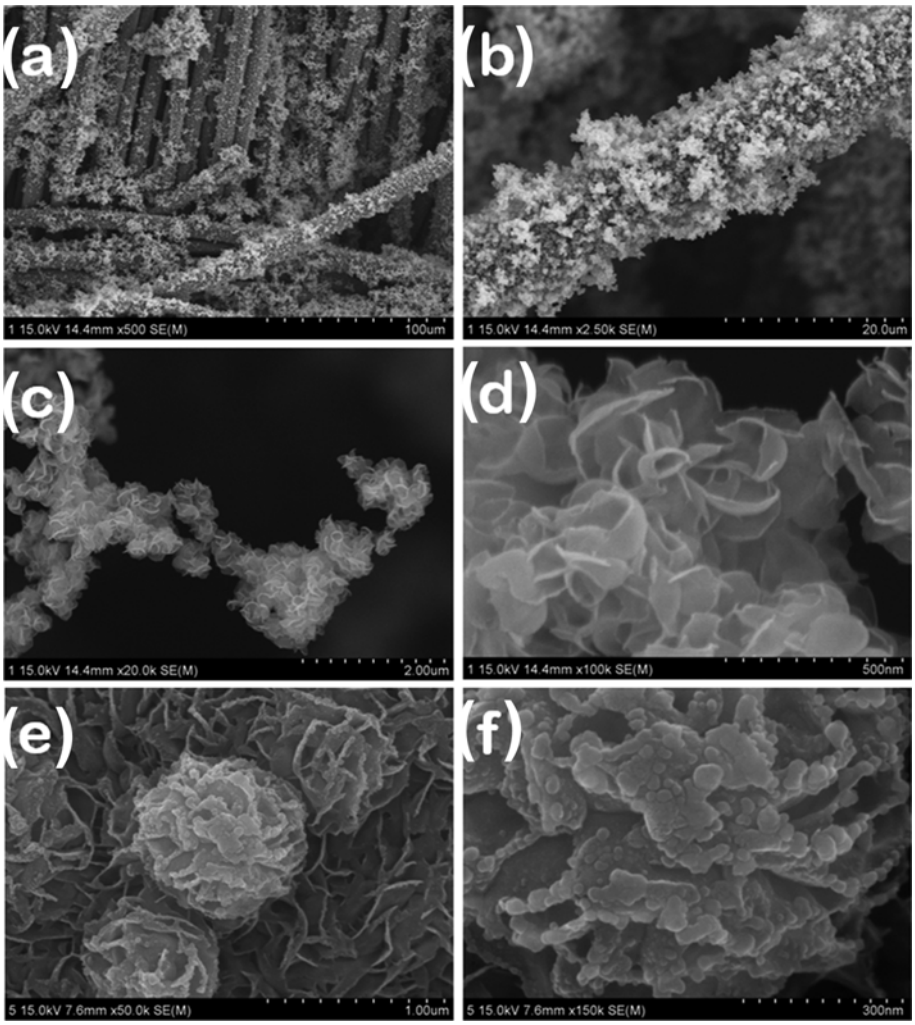

Fig. 3. FESEM micrographs of (a)-(d) as-grown MoS_2/CC; and (e)-(f) as deposited Ag@MoS_2/CC.

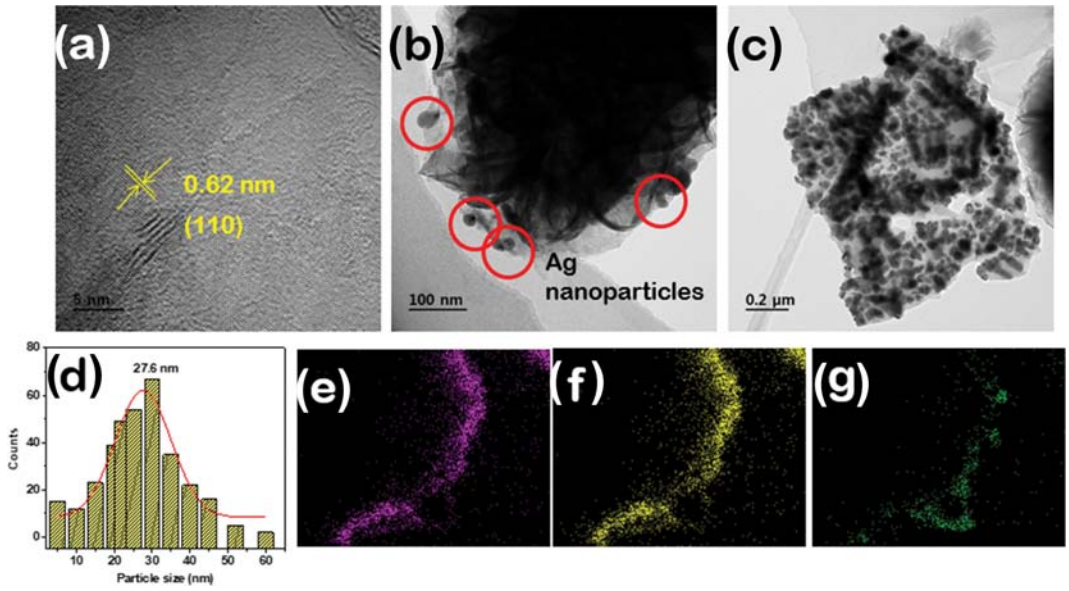

Fig. 4. HRTEM image of (a) MoS_2; TEM images of (b)-(c) Ag@MoS_2; (d) particle size distribution of Ag nanoparticles from TEM image; and energy dispersive elemental mapping of (e) Mo; (f) S; and (g) Ag mapping of as-deposited Ag@MoS_2/CC.

bly to form an irregular flower-like arrangement due to hydrothermal duration (Fig. 3(c)). The thin sheets appear translucent and have an average thickness of ~10-20 nm possibly because of the agglomeration of the sheets to form a flower-like structure (Fig. 3(d)). The CC substrate reduced the agglomeration of the MoS_2 microflowers, thus providing a large surface area for the photochemical reaction. In the case of the Ag@MoS_2/CC sample, the Ag particles show agglomeration and are distributed randomly on the surface of MoS_2 (Fig. 3(e)). The size of the Ag particles is between ~20-50 nm (Fig. 3(f)). The morphologies of pristine MoS_2 and Ag@MoS_2 were investigated by obtaining their high-resolution TEM (HRTEM) images (Fig. 4). Ag@MoS_2 was dispersed on a Cu-grid to obtain its elemental mapping. The HRTEM image of the MoS_2 nanosheets is shown in Fig. 4(a). The lattice fringe of MoS_2 was found to be 0.62 nm corresponding to the interlayer spacing of its (110) plane. Fig. 4(b) shows the Ag@MoS_2 nanosheets assembled in a microflower-like arrangement that is composed of individual nanosheets. Fig. 4(c) shows a single MoS_2 nanosheet with randomly distributed Ag nanoparticles on its surface. The Ag nanoparticles are pseudo-spherical and show agglomeration on the MoS_2 nanosheet. The average size of the Ag nanoparticles was calculated from the histogram of particle size distribution taken from TEM image in Fig. 4(c). Image J software was used for the calculation of the size of Ag nanoparticles. The average size of Ag nanoparticles distributed over MoS_2 nanosheet is around 27.6 nm (calculated from Gaussian fitting, Fig. 4(d)). The elemental mapping of Ag@MoS_2/CC shows the distribution of Mo, S, and Ag on the surface of the agglomerated MoS_2 nanosheets (Fig. 4(e)-(g)). The morphological analysis of MoS_2/CC and Ag@MoS_2/CC confirms the nanosheet-like morphology of MoS_2 assembling to microflowers and also the deposition of Ag nanoparticles on the MoS_2 surface is also established. The Brunauer-Emmett-Teller surface areas of the MoS_2 and Ag@MoS_2 powders were measured to investigate the effect of the active surface on the photochemical reaction. The measured surface area for MoS_2 was 19 m^2/g, while that for Ag@MoS_2 was about 27 m^2/g. The surface area of MoS_2 increased slightly after the deposition of Ag nanopar-

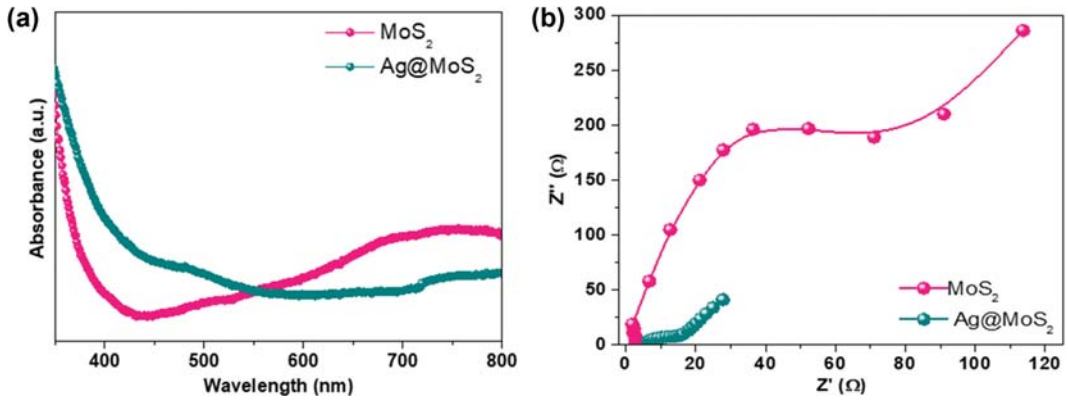

Fig. 5. (a) UV-visible absorption spectra of MoS_2 and Ag@MoS_2; and (b) EIS results of MoS_2/CC and Ag@MoS_2/CC.

ticles. This increase in the surface area is highly expected to be beneficial for the photochemical reaction.

2. Optical Band-gap and Charge Transfer Properties

The optical absorption of a material is directly related to its photocatalytic activity. Fig. 5(a) shows the UV-visible absorbance spectra of MoS_2 and Ag@MoS_2. For measuring the absorbance, the as-grown MoS_2 and as-deposited Ag@MoS_2 from carbon cloth was scratched and a suspension was prepared in water through ultrasonication. The prepared suspension was taken for UV-visible absorbance measurements. It can be observed from the figure that MoS_2 shows a broad absorbance peak in the visible region. The absorption was quite significant over the wavelength range of 500-700 nm. On the other hand, Ag@MoS_2 shows a strong absorption peak at 450-550 nm. Ag@MoS_2 shows a blue shift as compared to pristine MoS_2. The bandgap of pristine MoS_2 was calculated using the Kubelka-Munk equation: $(\alpha h\nu)^n = A(h\nu - E_g)$, where E_g is the band gap, ν is the frequency of light, h is Planck's constant, α is the coefficient of absorption, A is a constant, and n denotes the number of electronic transitions for the given semiconductor [41,42]. The bandgap of MoS_2 was calculated to be about 1.86 eV, which is similar to the values reported previously [43].

To understand the charge transfer resistance in both the prepared samples, the electrochemical impedance spectroscopy (EIS) (Fig. 5(b)) measurements of both MoS_2/CC and Ag@MoS_2/CC were carried out using an electrochemical workstation. The electrolyte used for the measurement was 0.1 M Na_2SO_4 with platinum sheet and Ag/AgCl as counter and reference electrode, respectively. The as-prepared samples were used as the working electrode. The measurement was performed at amplitude of 10 mV in the frequency range 100 kHz to 5 mHz. It can be observed from the figure that the Ag nanoparticle-decoration efficiently reduced the charge carrier recombination in MoS_2 by enhancing the mobility of its surface electrons. The improved charge separation efficiency of Ag@MoS_2/CC as compared to that of MoS_2/CC is also evident from its smaller electrochemical impedance spectrum curvature [44].

3. Photocatalytic Studies

The photocatalytic ability of MoS_2/CC and Ag@MoS_2/CC was evaluated by conducting a series of catalytic experiments under visible light irradiation. The absorbance maximum of RB, which is observed at 554 nm, was considered to monitor the degradation efficiency of the catalysts with respect to time. For the photochemical experiments, the MoS_2 microflowers were grown on a 4 cm×4 cm CC substrate. Since catalysis is a surface phenomenon, the MoS_2/CC and Ag@MoS_2/CC catalysts were immersed in a dye solution in a quartz beaker without light irradiation in order to attain the adsorption-desorption equilibrium on the catalyst surface. No change was observed in the concentration of RB even after 60 min. Hence, the photocatalysis process was initiated after 60 min with light irradiation. In the photocatalytic degradation of dyes, the adsorption of dye molecules on the catalyst surface accelerates the rate of initial catalytic reaction. The concentration profiles of both the catalysts for RB degradation are shown in Fig. 6(a). It can be observed that the MoS_2/CC and Ag@MoS_2/CC cat-

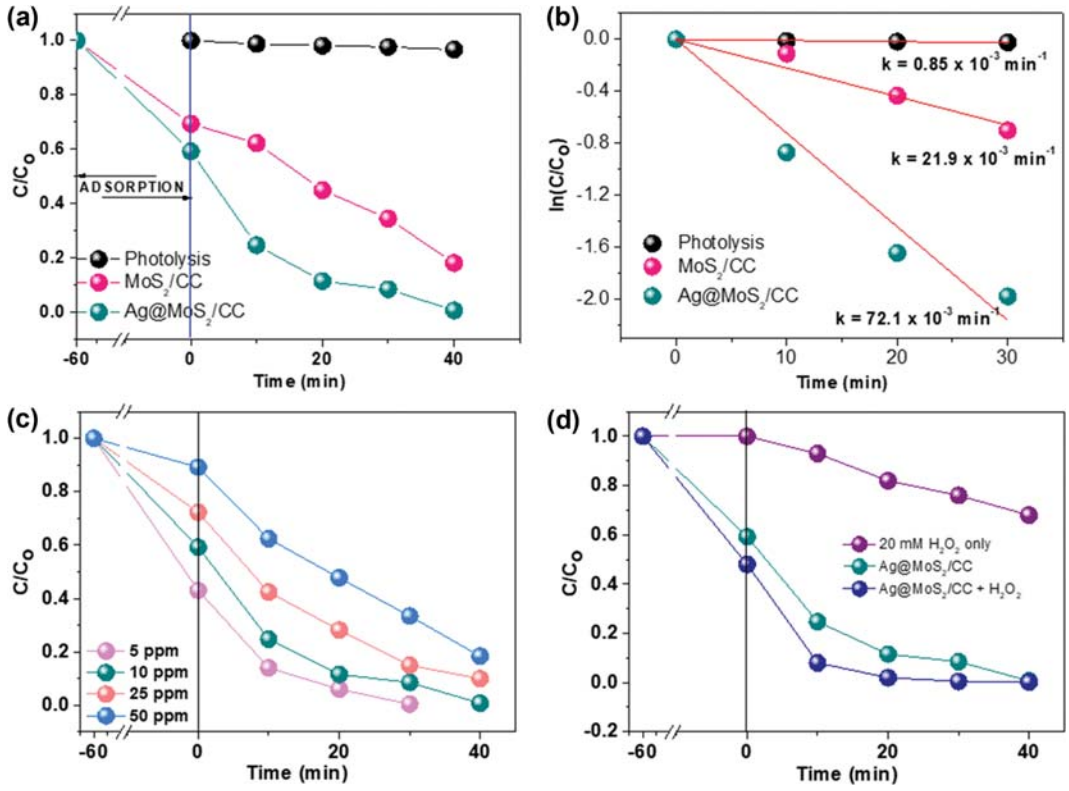

Fig. 6. (a) Concentration profiles; (b) Kinetic profiles for RB degradation of MoS_2/CC and Ag@MoS_2/CC; (c) Dye concentration effect (RB concentration: 5, 10, 25, 50 ppm); and (d) Oxidizer effect on the on degradation of RB with Ag@MoS_2/CC (H_2O_2 concentration: 20 mM).

alysts showed about 30 and 40% RB adsorption, respectively. The oxidation of RB in the presence of light without any catalyst was also carried out, which is named as photolysis in the figure. It was found that the dye degradation was negligible in the absence of the catalysts. Ag@MoS_2/CC shows significantly enhanced catalysis because of the presence of Ag nanoparticles, which promoted the photochemical reaction. The degradation efficiency is calculated by considering the adsorption point as initial value, marked as zero in the figure. MoS_2/CC shows slower RB degradation than Ag@MoS_2/CC with a degradation efficiency of about 74% in 40 min. On the other hand, in the presence of Ag@MoS_2/CC about 90% degradation was achieved in the first 20 min of irradiation and about 99% degradation at 40 min of light irradiation. The reaction kinetics of the catalysts were also studied and the corresponding plots are shown in Fig. 6(b). The reaction followed first-order kinetics in the first 30 min of irradiation. The first-order kinetic rate constants of MoS_2/CC and Ag@MoS_2/CC were calculated to be 21.9×10^{-3} and 72.1×10^{-3} min^{-1}, respectively, for the photochemical reaction time of 30 min. The plot shows the linear regression of the data points for 30 min because the regression coefficients for MoS_2/CC and Ag@MoS_2/CC obtained after 30 min were less than 95 and did not follow first-order kinetics. The kinetic rate constant of Ag@MoS_2/CC was about 3.3-times higher than that of MoS_2/CC, indicating that the decoration with Ag nanoparticles drastically increased the reaction rate of MoS_2/CC. The linear regression coefficients of both Ag@MoS_2/CC and MoS_2/CC were greater than 95. Furthermore, Ag@MoS_2/CC was investigated for the degradation of RB having varying dye concentration. In addition, to enhance the catalytic activity, experiments with H_2O_2 were conducted.

The standard concentration of RB was varied and the catalytic activity in the presence of Ag@MoS_2/CC under visible light irradiation was carried out following the same experimental process. Fig. 6(c) displays the results of adsorption and degradation of RB for different concentrations 5, 10, 25, and 50 ppm. It is observed that with lower RB concentration than 10 ppm, the adsorption is increased along with the degradation efficiency (RB=5 ppm). The adsorption decreases with increase in RB concentration and also affects the degradation process. The degradation with 5, 10, 25, and 50 ppm is about 99% in 30 min, 99%, 87.5%, and 79% in 40 min, respectively. The lowest RB dye concentration of 5 ppm shows the highest degradation efficiency due to enhanced adsorption. Similar observations have been reported by Kwon et al. [34]. To enhance the activity in the existing process, a strong oxidizer such as hydrogen peroxide (H_2O_2) was added to the dye solution and the experiment in presence of the designed catalyst was carried out. It is well-reported that H_2O_2 can photo-produce hydroxyl radicals due to direct self-photocleavage [45]. Thus, in the present study a fixed concentration of 20 mM of 30% H_2O_2 was taken and catalysis was conducted in the presence and absence of Ag@MoS_2/CC as shown in Fig. 6(d). About 30% degradation of RB takes place in the presence of 20 mM H_2O_2 only, whereas more than 95% degradation happens in the first 10 min of the photocatalytic process with catalyst and 20 mM H_2O_2. This can be associated with the increased amount of hydroxyl radical generation with the addition of H_2O_2 that enhances the photochemical reactivity while decreasing the

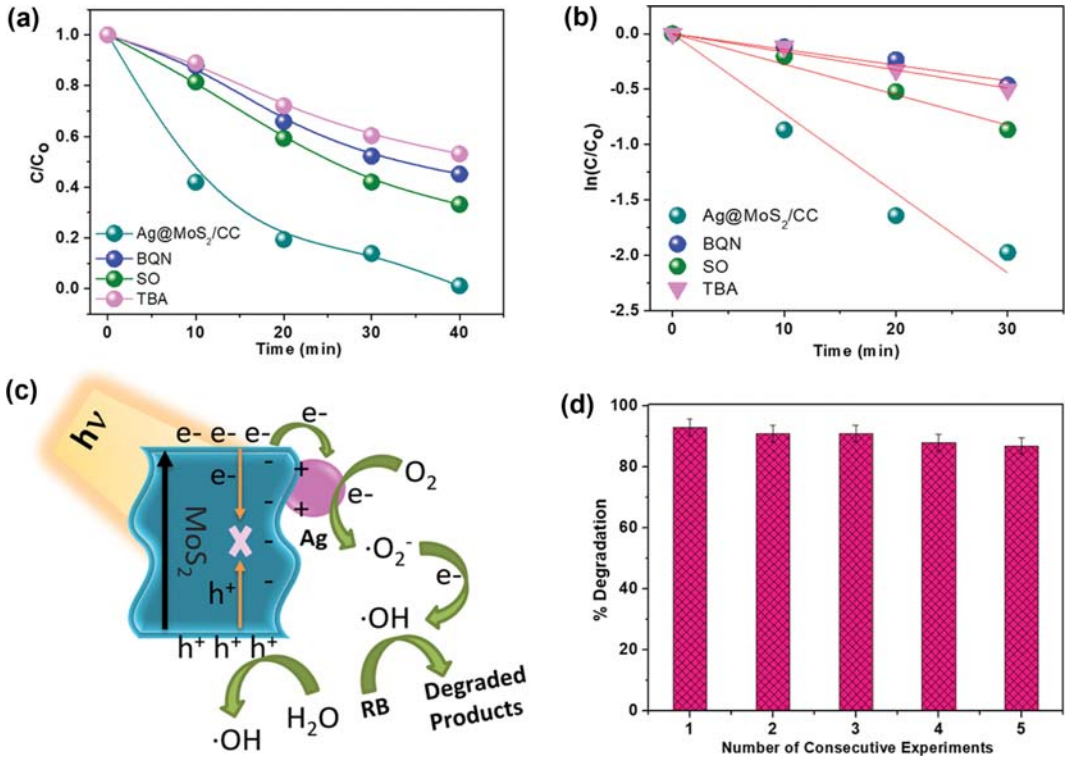

Fig. 7. (a) Concentration profiles and (b) kinetic profiles of the Ag@MoS_2/CC catalyst with and without scavengers; (c) Photocatalytic mechanism and (d) reusability experiments of the Ag@MoS_2/CC catalyst (SO-sodium oxalate; BQN-benzoquinone; and TBA-tert-butylalcohol).

reaction time.

4. Identification of Reactive Species and Reusability Experiments

To identify the major reactive species involved in the photochemical reaction, scavenger experiments were carried out using the $Ag@MoS_2$/CC catalyst with the CC dimensions of 4 cm×4 cm. The chemical reagents used for scavenging the photochemical reactive species ·OH, $\cdot O^{2-}$, and h^+ were tert-butylalcohol (TBA), benzoquinone (BQN), and sodium oxalate (SO), respectively. For each reaction, the amount of the scavenger used was about 15 mM. The scavengers were introduced into the reaction system with light irradiation once the adsorption-desorption equilibrium was attained. The degradation efficiency of the 4 cm×4 cm $Ag@MoS_2$/CC catalyst with and without scavengers was compared to investigate the effect of the reactive species on the photochemical reaction and the results are shown in Fig. 7(a). The addition of SO inhibited the reaction. The incorporation of TBA inhibited the reaction significantly. Slight inhibition was also observed with the addition of BQN. Comparing the reaction inhibitions, most of the reaction occurred because of hydroxyl radicals and superoxide radicals. The hydroxyl radicals significantly contributed to the degradation of the dye molecules in the reaction system. The superoxide radicals also played a major role in the conversion of the hydroxyl radicals at the surface of $Ag@MoS_2$. However, the rapid oxidative conversion to hydroxyl radicals suppressed the reactivity of the superoxide radicals. This was possible only when the surface of the catalyst was electron populated. The first-order kinetics of the scavenger reactions of the catalysts was plotted and the rate constants were calculated from their linear regressions, as shown in Fig. 7(b). The kinetic rate constants of the photochemical reactions carried out in the presence of BQN, SO, and TBA were 15.1×10^{-3}, 27.5×10^{-3}, and 15.5×10^{-3} min^{-1}, respectively. These results indicate that there was significant competition between the superoxide radicals and also the formation of oxidative reactive hydroxyl species. The reaction rate of the catalyst with the hydroxyl radical scavenger (TBA) was 4.6-times lower than that of the pristine one. Note that there was significant competition between the generation of radicals and the degradation process. Hence, the hydroxyl radicals and superoxide radicals participated actively in the reaction for initiating the oxidative chain reaction, which ultimately contributed to the degradation process. Photon processing was fast at the catalyst surface because of its dense electron population through silver nanoparticles.

By comparing the photocatalytic efficiency of MoS_2/CC and $Ag@MoS_2$/CC, it was found that the Ag nanoparticles affected the catalytic process by absorbing the visible-light photons. The scavenger experiments also confirmed the dense electron population at the surface of $Ag@MoS_2$/CC. The improved dye degradation efficiency of free-standing $Ag@MoS_2$/CC as compared to that of MoS_2/CC can be attributed to the presence of Ag nanoparticles in it. The photocatalytic mechanism of $Ag@MoS_2$ involved the alignment of its Fermi level when both the Ag nanoparticles and MoS_2 were in contact with each other. Electron transfer in $Ag@MoS_2$/CC occurred through the space charge region, which was formed because of the difference (of about 0.8-1.5 eV) in the Fermi levels of MoS_2 (~4.0-4.7 eV) and the Ag nanoparticles (~5.5 eV) [46]. A depletion/space charge region was formed between the Ag nanoparticles and MoS_2, which resulted in band bending because the surfaces of MoS_2 and the Ag nanoparticles were occupied with negative and positive charges, respectively. When light was irradiated on the surface of $Ag@MoS_2$, the incident photons were absorbed and excited the surface with photogenerated electron-hole pairs followed by the channeling of electrons from the conduction band of MoS_2 to the surface of the Ag nanoparticles because of their Fermi level offset [35]. The Ag nanoparticles acted as a sink for electron collection, making the surface heavily populated with the transferred electrons and hence faster radical generation processing. The transfer of electrons competed with the formation of oxidative reactive species, thus accelerating the reaction. This also hindered the process of recombination at the MoS_2 surface which was efficiently utilized for the photochemical reaction, as shown in Fig. 7(c).

In this study the catalysts were grown on a CC substrate; thus, it could be easily reused. Catalyst reusability is crucial for photocatalysis [47]. The reusability of $Ag@MoS_2$/CC was evaluated and the corresponding results are shown in Fig. 7(d). Re-run experiments were carried out with the same catalyst for five consecutive cycles. After each experiment, the free standing catalyst was taken out and air dried for 12 h at 120 °C to remove the dye molecules and adsorbed water molecules from the catalyst surface. The recycling process negligibly affected the degradation rate of the catalyst with a loss of about 3-4%. This indicates that the material was quite stable. Hence, the use of CC as the catalyst support not only eases the process of catalyst separation but also enhances the surface reactivity by reducing the inter-agglomeration of particles during the photochemical reaction. Similar combinations of MoS_2 with other noble metals, such as gold (Au), are also reported in literature as powder photocatalyst [22] and sensing material [48], where the former is less popular. To compare, the gold-modified MoS_2 nanosheets system was able to degrade about 30% of rhodamine B under visible light, which is much lower than the present $Ag@MoS_2$/CC photocatalytic system [22]. Flexible support-based catalysts are beneficial for developing catalytic membranes for environmental applications.

CONCLUSION

A visible light-active free standing $Ag@MoS_2$ photocatalyst was developed on a flexible CC substrate using a hydrothermal and chemical reduction method. The CC substrate increased the active surface area of the photocatalyst by reducing the inter-agglomeration of the MoS_2 particles and opening more active catalytic sites. The physicochemical characterizations confirmed the formation of $Ag@MoS_2$/CC with MoS_2 microflowers composed of thin nanosheets attached to the CC. The EIS studies showed that the incorporation of Ag nanoparticles enhanced the charge transfer process at the surface of MoS_2. The improved RB degradation efficiency of the $Ag@MoS_2$/CC catalyst can be attributed to the presence of silver nanoparticles on MoS_2 surface. The Ag nanoparticles increased the catalytic efficiency of $Ag@MoS_2$/CC by attracting electrons from MoS_2, making the catalyst surface electron populated, which played a key role in the photochemical reaction by hindering the recombination process. Noble metal-based nanocomposite structures grown on flexible substrates can ease the catalytic process and can be effectively used for environmental applications.

ACKNOWLEDGEMENTS

The authors thank the National Research Foundation of Korea (NRF-2015M3A7B 4050 424) and the Korea Research Fellowship Program (KRF grant no. 2018H1D3A1A02074832) for support. The authors also thank Korea Basic Science Institute (KBSI) at Gwangju center for SEM and TEM analyses.

REFERENCES

1. J. Chang, L. Zhang and P. Wang, *Environ. Sci. Nano*, **5**, 811 (2018).
2. H. Li, J. Li, A. Thomas and Y. Liao, *Adv. Funct. Mater.*, **29**, 1904785 (2019).
3. N. T. M. Tho, B. T. Huy, D. N. N. Khanh, H. N. N. Ha, V. Q. Huy, N. T. T. Vy, D. M. Huy, D. P. Dat and N. T. K. Phuong, *Korean J. Chem. Eng.*, **35**, 2442 (2018).
4. T. Li, T. Sun, T. B. Aftab and D. Li, *Korean J. Chem. Eng.*, **34**, 1199 (2017).
5. M. A. E. Barakat, R. Kumar, N. H. A.l-Makishah, A. A. Neamtallah and Z. O. Alafif, *Korean J. Chem. Eng.*, **36**, 1281 (2019).
6. W. Li, L. Wang, Q. Zhang, Z. Chen, X. Deng, C. Feng, L. Xu and M. Sun, *J. Alloys Compd.*, **808**, 151681 (2019).
7. Y. Cui, L. Yang, M. Meng, Q. Zhang, B. Li, Y. Wu, Y. Zhang, J. Lang and C. Li, *Korean J. Chem. Eng.*, **36**, 236 (2019).
8. S.-S. Lee, B. T. Huy, N. T. K. Phuong, D. K. Tung and Y.-I. Lee, *Korean J. Chem. Eng.*, **36**, 1716 (2019).
9. M. G. Peleyeju and O. A. Arotiba, *Environ. Sci. Water Res. Technol.*, **4**, 1389 (2018).
10. K. Qiu, J. Zhou, P. Qi, Q. Zhou, X. Gao and Z. Luo, *Korean J. Chem. Eng.*, **34**, 2383 (2017).
11. S. Han, G.-S. Chae and J. S. Lee, *Korean J. Chem. Eng.*, **33**, 1799 (2016).
12. X. Zheng, D. Li, X. Li, L. Yu, P. Wang, X. Zhang, J. Fang, Y. Shao and Y. Zheng, *Phys. Chem. Chem. Phys.*, **16**, 15299 (2014).
13. C. Ding, J. Shi, Z. Wang and C. Li, *ACS Catal.*, **7**, 675 (2017).
14. M. A. Mutalib, F. Aziz, N. A. Jamaludin, N. Yahya, A. F. Ismail, M. A. Mohamed, M. Z. M. Yusop, W. N. W. Salleh, J. Jaafar and N. Yusof, *Korean J. Chem. Eng.*, **35**, 548 (2018).
15. X. Liu, Z. Zhou, Y. Lu, T. Wang, P. Huo and Y. Yan, *Adv. Powder Technol.*, **30**, 1043 (2019).
16. H. Robatjazi, S. M. Bahauddin, C. Doiron and I. Thomann, *Nano Lett.*, **15**, 6155 (2015).
17. W. Wang, M. O. Tadé and Z. Shao, *Chem. Soc. Revs.*, **44**, 5371 (2015).
18. Y.-S. Cho, H. J. Lee and S. Sung, *Korean J. Chem. Eng.*, **37**, 1071 (2020).
19. M. Isleyen, E. S. Ilkme and G. S. P. Soylu, *Korean J. Chem. Eng.*, **34**, 1786 (2017).
20. H. Wang, C. Li, P. Fang, Z. Zhang and J. Z. Zhang, *Chem. Soc. Revs.*, **47**, 6101 (2018).
21. B. Khan, F. Raziq, M. Bilal Faheem, M. Umar Farooq, S. Hussain, F. Ali, A. Ullah, A. Mavlonov, Y. Zhao, Z. Liu, H. Tian, H. Shen, X. Zu, S. Li, H. Xiao, X. Xiang and L. Qiao, *J. Hazard. Mater.*, **381**, 120972 (2019).
22. H. Song, L. Wei, C. Chen, C. Wen and F. Han, *J. Catal.*, **376**, 198 (2019).
23. L. Huang, L. Ai, M. Wang, J. Jiang and S. Wang, *Int. J. Hydrogen Energy*, **44**, 965 (2019).
24. M. Behtaj Lejbini and P. Sangpour, *Optik*, **177**, 112 (2019).
25. S. Jia, M. Xu, S. Chen, J. Yan, J. Yun, Z. Deng, Z. Zhang, W. Zhao, Y. Wang and X. Ma, *Mater. Lett.*, **236**, 697 (2019).
26. Y. Kang, Y. Gong, Z. Hu, Z. Li, Z. Qiu, X. Zhu, P. M. Ajayan and Z. Fang, *Nanoscale*, **7**, 4482 (2015).
27. H. Wang, S. B. Naghadeh, C. Li, L. Ying, A. L. Allen and J. Z. Zhang, *Sci. China Mater.*, **61**, 839 (2018).
28. I. Olvera-Rodríguez, R. Hernández, A. Medel, C. Guzmán, L. Escobar-Alarcón, E. Brillas, I. Sirés and K. Esquivel, *Sep. Purif. Technol.*, **224**, 189 (2019).
29. H. Zheng, P. Niu and Z. Zhao, *RSC Adv.*, **7**, 26943 (2017).
30. E. H. Jeon, S. Yang, Y. Kim, N. Kim, H.-J. Shin, J. Baik, H. S. Kim and H. Lee, *Nanoscale Res. Lett.*, **10**, 361 (2015).
31. H.-J. Chen, Y.-L. Yang, M. Hong, J.-G. Chen, G.-Q. Suo, X.-J. Hou, L. Feng and Z.-G. Chen, *Sustain. Mater. Techno.*, **21**, e00105 (2019).
32. L. Luo, X. Shen, L. Song, Y. Zhang, B. Zhu, J. Liu, Q. Chen, Z. Chen and L. Zhang, *J. Alloys Compd.*, **779**, 599 (2019).
33. X. Li, Y. Sun, T. Xiong, G. Jiang, Y. Zhang, Z. Wu and F. Dong, *J. Catal.*, **352**, 102 (2017).
34. D. Kwon and J. Kim, *Korean J. Chem. Eng.*, **37**, 1226 (2020).
35. A. J. Cheah, W. S. Chiu, P. S. Khiew, H. Nakajima, T. Saisopa, P. Songsiriritthigul, S. Radiman and M. A. A. Hamid, *Catal. Sci. Technol.*, **5**, 4133 (2015).
36. M. Li, Z. Cui and E. Li, *Ceram. Int.*, **45**, 14449 (2019).
37. S. Adhikari, H. H. Lee and D.-H. Kim, *Chem. Eng. J.*, **391**, 123504 (2020).
38. J. Cao, J. Zhou, Y. Zhang and X. Liu, *Sci. Reps.*, **7**, 8825 (2017).
39. H. Liu, X. Chen, L. Deng, X. Su, K. Guo and Z. Zhu, *Electrochim. Acta*, **206**, 184 (2016).
40. S. Adhikari, A. Banerjee, N. K. Eswar, D. Sarkar and G. Madras, *RSC Adv.*, **5**, 51067 (2015).
41. X. Bai, Y. Du, X. Hu, Y. He, C. He, E. Liu and J. Fan, *Appl. Catal. B: Environ.*, **239**, 204 (2018).
42. H.-R. Jung, K. N. Kim and W.-J. Lee, *Korean J. Chem. Eng.*, **36**, 807 (2019).
43. J. Wang, Z. Guan, J. Huang, Q. Li and J. Yang, *J. Mater. Chem. A*, **2**, 7960 (2014).
44. A. Ali, F. A. Mangrio, X. Chen, Y. Dai, K. Chen, X. Xu, R. Xia and L. Zhu, *Nanoscale*, **11**, 7813 (2019).
45. M. Feilizadeh, F. Attar and N. Mahinpey, *Can. J. Chem. Eng.*, **97**, 2009 (2019).
46. X.-Q. Qiao, Z.-W. Zhang, F.-Y. Tian, D.-F. Hou, Z.-F. Tian, D.-S. Li and Q. Zhang, *Cryst. Growth Des.*, **17**, 3538 (2017).
47. L. Yang, Y. An, B. Dai, X. Guo, Z. Liu and B. Peng, *Korean J. Chem. Eng.*, **34**, 476 (2017).
48. J. Wang, Q. Zhou, Z. Lu, Z. Wei and W. Zeng, *Appl. Surf. Sci.*, **124**, 490 (2019).